

Intensity and velocity oscillations in a flaring active region

David C. L. Millar¹, Lyndsay Fletcher^{1,2} and Jayant Joshi³

¹*School of Physics & Astronomy, University of Glasgow, Glasgow G12 8QQ, UK*

²*Roseland Centre for Solar Physics, University of Oslo, P.O.Box 1029 Blindern, NO-0315 Oslo, Norway*

³*Indian Institute of Astrophysics, II Block, Koramangala, Bengaluru 560 034, India*

Accepted 2023 October 30. Received 2023 October 5; in original form 2023 July 18

ABSTRACT

Chromospheric oscillations can give us insight into the physical environment in the solar atmosphere, both in quiet Sun and flaring conditions. Many authors have reported increases in the prevalence of 3-minute oscillations which are thought to be excited by events which impact the chromosphere such as flares. In this study, we utilized the Ca II 8542 Å line to study the oscillatory behaviour of the chromosphere in an active region which underwent two B-class flares. We analysed oscillations in both intensity and velocity, and found different behaviours in both. Intensity oscillations were most prevalent over the umbrae of sunspots and magnetic pores in the active region, and the extent of the area which contained significant oscillations was found to decrease when comparing times after the flares to before. By measuring the evolution of the magnetic field, we found that this could be because the areas surrounding the umbrae were becoming more ‘penumbral’ with an increase to the magnetic field inclination. Velocity oscillations were found across the active region both before and after the flares but were observed clearly in areas which were brightened by the second flare. By comparing to EUV imaging, it was seen that strong chromospheric velocity oscillations with 3–4-minute periods occurred at the same time and location as a flare loop cooling 30 min after the second flare peak. This could be evidence of disturbances in the loop exciting a response from the chromosphere at its acoustic cut-off frequency.

Key words: Sun: chromosphere – Sun: flares – Sun: oscillations.

1 INTRODUCTION

The study of oscillations can be a powerful window into the mechanics of a solar flare, for example in the widely studied field of quasi periodic pulsations (QPP) – see Van Doorsselaere, Kupriyanova & Yuan (2016) for a review. QPPs have been observed across all wavelengths; from radio (Inglis et al. 2016) to gamma-rays (Nakariakov et al. 2010); with time-scales ranging from sub-second (Tan & Tan 2012) to several minutes (Milligan et al. 2017). The myriad of characteristics of these periodic signals during flares has led to many different proposed physical mechanisms to explain them. These include MHD effects such as kink or sausage modes, and a repetitive energy injection such as self-oscillatory ‘dripping’ magnetic reconnection.

The study of oscillations during flares at chromospheric wavelengths is interesting because there are already quiescent oscillations observed in the quiet Sun chromosphere with periods of a few minutes, and we have the opportunity to study their behaviour in response to rapid flare-related changes in the chromosphere (e.g. temperature, magnetic field orientation). The quiescent chromospheric oscillations are often referred to as ‘three-minute oscillations’ and have been observed in intensity and velocity data since the 1970s (Bhatnagar & Tanaka 1972), being particularly strong over sunspots (Khomenko &

Collados 2015). Their origin is thought to be linked to the convective motion underneath the photosphere, which drives waves upwards into the chromosphere. It was initially proposed that the ~3 minute period is caused by the waves becoming trapped in a ‘chromospheric cavity’ between the temperature minimum and the transition region (Uchida & Sakurai 1975), however, another prevalent explanation comes from the acoustic cut-off frequency of the chromospheric medium. In regions of high magnetic field strength, photospheric disturbances travel along magnetic field lines as magnetoacoustic gravity waves (Bel & Leroy 1977), and frequencies below the cut-off frequency ω_c are filtered out (Lamb 1909). The value for cut-off frequency depends on the gravitational acceleration g , the sound speed in the plasma c_s , and the angle between the gravitational and magnetic fields θ :

$$\omega_c = \frac{\gamma g \cos \theta}{2c_s}. \quad (1)$$

Here, γ is the ratio of specific heats, and using typical values for the temperature minimum region gives $\omega_c \approx 0.03 \text{ rad s}^{-1}$, corresponding to periods of $P \approx 200 \text{ s}$ (Fleck & Schmitz 1991).

It has been proposed that a resonance at the cut-off frequency is a natural response of the chromosphere to excitation (Fleck & Schmitz 1991), and it could be excited by different sources such as the underlying photospheric driver, or energy injection in the form of ‘velocity kicks’ (Kalkofen et al. 1994; Chae & Goode 2015). Such enhancements of the 3-minute oscillations have been

* E-mail: david.millar.2@glasgow.ac.uk

reported in past observational studies, for example Milligan et al. (2017) found ~ 3 minute oscillations during the impulsive phase of an X-class flare in full-disk Ly α and UV emission. A similar 3-minute periodicity was found in Ly α by Li et al. (2020), but with an accompanying 1-minute signal. This 1-minute signal was thought to be evidence of magnetic dripping or an unidentified MHD wave at the flare footpoints. Kwak et al. (2016) reported chromospheric velocity oscillations after detecting a downflow event in the upper atmosphere, which could have resulted in a velocity kick. Farris & McAteer (2020) mapped the strength of 3-minute signals in UV wavelengths, finding localized areas of increased power which were cospatial with hard x-ray emission during a flare. Excitation of sunspot oscillations has been observed in flaring regions (Kosovichev & Sekii 2007; Sych et al. 2009), with Sych et al. (2009) reporting increases to 3-minute power in the lead-up to a flare.

In this paper, we present analysis of a data set from the CRISP imaging spectro-polarimeter (CRISP; Scharmer et al. 2008) instrument of the Swedish Solar Telescope (SST; Scharmer et al. 2003a), captured on 2013 June 13. The observations feature an active region which underwent two B-class flares in quick succession. We sought to investigate the oscillatory signals which were present before and after the flare events, in both intensity and velocity data. Similar analyses were carried out in Millar, Fletcher & Milligan (2021) with another CRISP data set, however, in that event only intensity oscillations were studied, in the Ca II 8542 Å and H α spectral lines. In that study, the oscillatory behaviour of the chromosphere around a sunspot was seen to change after an M1-class flare occurred in the active region. This study expands upon these results, by analysing velocity oscillations in addition to intensity, and using a spectropolarimetric data set, giving us the opportunity to measure the chromospheric and photospheric magnetic fields.

The flares and CRISP data set are detailed in Section 2, before describing the analytical methods in Section 3. The results of the oscillatory analyses are presented in Section 4. We investigate the evolution of the atmosphere in Section 5. A discussion of the results is given in Section 6 and we conclude in Section 7.

2 DESCRIPTION OF FLARES AND DATA SETS

The flares occurred on 2013 June 13 in active region NOAA 11768, which was west of disc centre, with $\mu = 0.915$. The flares were of GOES classes B7.2 and B9.3, starting at 09:20 and 09:55 UTC, respectively. A GOES timeline can be seen in Fig. 1, which encompasses the time of the CRISP observation window (08:21–11:00). CRISP measured two spectral lines: Fe I 5250 Å sampled over $-0.2 \text{ \AA}/+0.24 \text{ \AA}$ in 0.04 Å steps; and Ca II 8542 Å covering $\pm 0.5 \text{ \AA}$ in 0.1 Å steps. These sample the photosphere and chromosphere, respectively, with full Stokes polarimetry. The observations were obtained with 8 ms exposure and ten exposures were acquired per line position and per polarimetric state. Along with narrow-band spectropolarimetric observations, wide-band images were obtained using filters with 3.3 and 9.3 Å band-pass centred around the Fe I 5250 Å and Ca II 8542 Å lines, respectively. The total cadence of these observations is ~ 31 s and the duration of the complete time series is 2 h 39 min. The CRISP plate scale is 0.057 arcsec per pixel. High spatial resolution observations were obtained by a combination of good seeing conditions and the high-quality adaptive optics system (Scharmer et al. 2003b). We used the multiobject multiframe blind deconvolution (MOMFBD; van Noort, Rouppe van der Voort & Löfdahl 2005) method for image restoration, and the data were processed using the CRISP data processing pipeline (de la Cruz Rodríguez et al. 2015).

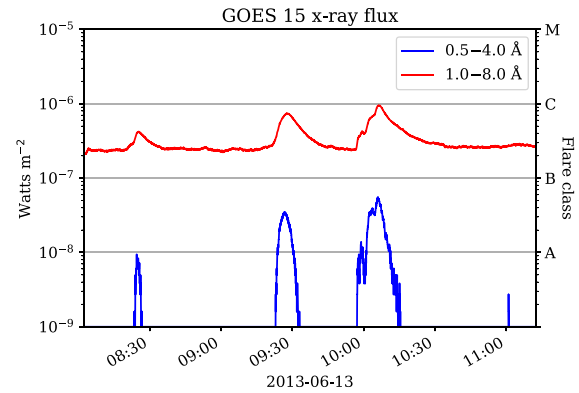


Figure 1. X-ray flux in two wavelength bands measured by the GOES-15 spacecraft during the time of the CRISP observation. Only the two flares which began at 09:20 and 09:55 occurred within the target active region. The corresponding flare class is shown on the right axis, determined by the 1.0–8.0 Å flux.

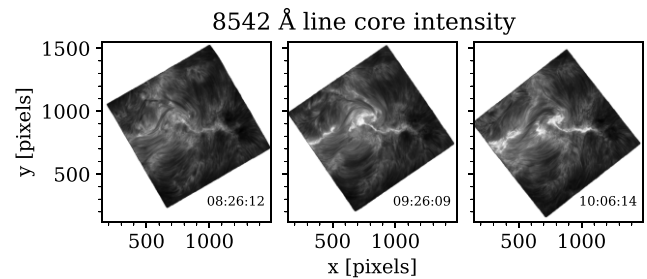


Figure 2. Images from Ca II 8542 Å core, showing the active region at the start of the CRISP data set, and at the times of the two flares. One pixel is 0.057 arcsec.

We show in Fig. 2 some Ca II 8542 Å line core images from the beginning of the observations, and at the time of each flare. The images are co-aligned, with solar north pointing upwards, meaning the image borders rotate and drift slightly, but the same solar location remains at the same image pixels. As seen in the first image, before the flares, the bright band extending along the middle of the field of view, which went on to become a flare ribbon, was already visible. The first flare caused brightening mostly close to the centre of the field of view, while the second flare ignited the horizontal band, forming the flare ribbon which is connected to a group of sunspots on the right. This group of underlying sunspots and pores can be seen in Fig. 3, in an intensity image from the wing of Fe I 5250 Å. The main features will be referred to as sunspots A–D, in order from right to left, to describe the locations of interesting results.

In Figs 4 and 5, we show examples of Stokes profiles in the Ca II 8542 Å and Fe I 5250 Å spectral windows. These are both drawn from the same pixel at $x = 1000$, $y = 825$ which is within one of the sites of flare heating, to the east of sunspot C. The Stokes I profile for Ca II 8542 Å in Fig. 4 shows strong emission due to the heating. The Q and U lines do not have clear shapes, while the V data are much clearer. This is due to low signal in the Q and U data. The photospheric Fe I 5250 Å line is in absorption, with the other Stokes parameters looking much clearer than their Ca II 8542 Å counterparts. The noise level of the Stokes Q , U , and V observations in the Fe I 5250 Å line is 3.1×10^{-3} , 3.0×10^{-3} , and 2.2×10^{-3} , respectively. For the Ca II 8542 Å observations, Stokes Q , U , and V noise level is 2.0×10^{-3} , 2.2×10^{-3} , and 2.8×10^{-3} , respectively.

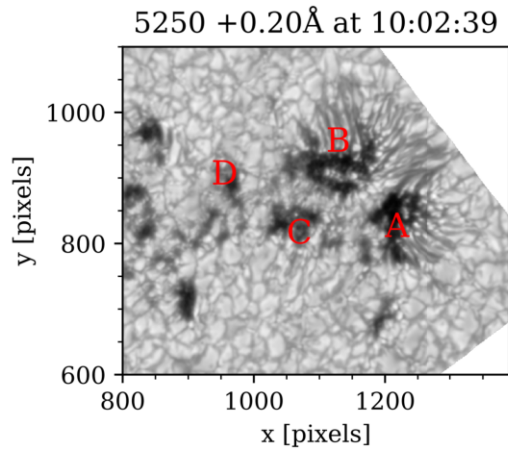


Figure 3. Fe I 5250 Å image showing the underlying sunspots and pores of the active region. The largest sunspots are labelled as they will be referred to throughout this paper.

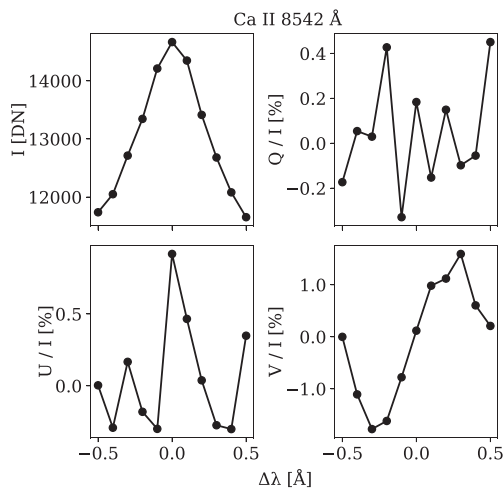


Figure 4. Example Stokes profiles for the Ca II 8542 Å line from a pixel in one of the flare ribbons. The Q, U, and V profiles have been normalized by the I continuum.

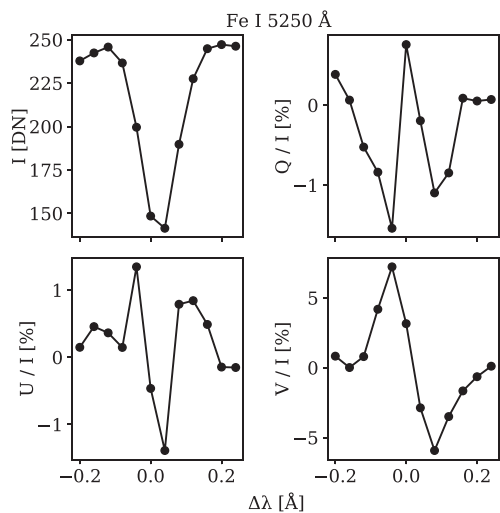


Figure 5. Example Stokes profiles for the Fe I 5250 Å line, in the same pixel as Fig. 4. The Q, U, and V profiles have been normalized by the I continuum.

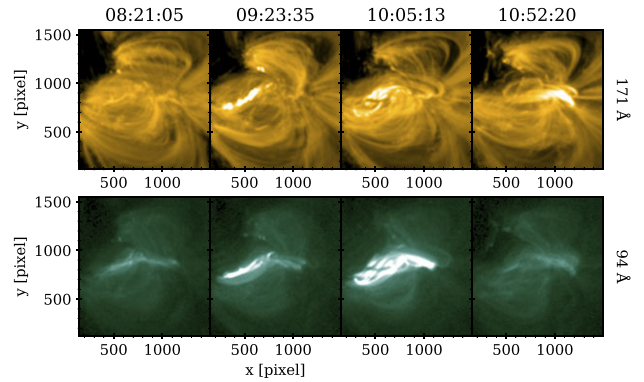


Figure 6. Images from the 171 Å and 94 Å channels of SDO/AIA, spanning the length of the CRISP data set and covering the same field of view. All subfigures from each channel have equal colour scales.

We can see in the Ca II 8542 Å context imaging in Fig. 2 that the area connecting the bright points to the left and in the centre of the field of view is complex, with a dark filament-like structure visible in the latter two panels of this figure. This structure moves around a lot during the flare activity, and it may have participated in magnetic reconnection between flare footpoints, as its shape is outlined in EUV wavelengths seen in Fig. 6 which contains images from the Atmospheric Imaging Assembly (AIA; Lemen et al. 2012) onboard the Solar Dynamics Observatory (SDO; Pesnell, Thompson & Chamberlin 2012). AIA captures the solar disk in UV/EUV wavebands, and here, we show images from the 171 Å and 94 Å channels. The 171 Å channel, shown in the upper row of Fig. 6, is sensitive to temperatures of $\log T \sim 5.8$ and is used to study quiet coronal loops, while the 94 Å channel (lower row) captures much hotter plasma at $\log T \sim 6.8$, and can therefore show flaring regions. The first three panels of each row closely match the times of the Ca II 8542 Å images in Fig. 2, while the fourth time instance is well after the second flare. In 171 Å, the flare ribbon is initially seen followed by flare loop emission, whereas 94 Å appears dominated by complex loops that cool into the 171 Å channel.

We aligned the AIA channels, the Helioseismic Magnetic Imager (HMI) continuum, and magnetogram data to the SST/CRISP Fe I 5250 Å wideband observations. To achieve this alignment, we utilized an automated procedure developed by Rob Rutten. This alignment tool is publicly available.¹ To ensure precision in aligning the SDO channels, the procedure involved the retrieval of two sets of SDO cutouts. One set focused on the smaller SST wideband target area, captured at full cadence, while the other set encompassed larger regions (700×700 arcsec) around the solar disc's centre, acquired at a lower cadence. The latter set was used to determine offsets between various channels through the cross-correlation of smaller subfields and by considering height-of-formation differences in an iterative manner. For a more comprehensive explanation, please see Rutten (2020). The AIA and HMI data sets were resampled from their original pixel scale to a crisp pixel scale of 0.057 arcsec. The alignment procedure considers temporal proximity between SDO and SST images using a nearest-neighbour selection method.

¹<https://robrutten.nl/rridl/00-README/sdo-manual.html>

3 METHODS

3.1 Spectrum fitting

In order to search for oscillatory signatures in the observed timeseries, we used the spectrum fitting method which has been used previously by many authors in various forms (Inglis, Ireland & Dominique 2015; Auchère et al. 2016; Threlfall, De Moortel & Conlon 2017; Battams, Gallagher & Weigel 2019). The method involves creating a Fourier power spectrum from a timeseries and modelling its shape to characterize periodic behaviour.

3.1.1 The Fourier power spectrum

The Fourier power spectrum (FPS) measures the strength of periodic signal as a function of frequency, f , and is obtained from an initial timeseries by the following method: the input signal is normalized by subtracting its mean and dividing by its standard deviation; a Hann window function is applied to the normalized signal; a fast Fourier transform is applied; the negative frequency part of the spectrum is removed; the absolute value squared is taken; finally the spectrum is normalized by the variance of the original signal.

3.1.2 Spectrum models

For this study, we adopt three models to describe the observed Fourier spectra: red-noise (M1), Gaussian bump (M2), and kappa function (M3). The first model, M1, is a power law which flattens off at high frequencies (due to photon counting noise), and is described by

$$M1 = Af^{-\alpha} + C. \quad (2)$$

A and C are constants, and α is the power-law index. The second model, M2, is similar to the first but has three additional parameters which describe a Gaussian bump in the spectrum above the red-noise background:

$$M2 = M1 + B_G \exp\left(\frac{-(\ln f - \beta)^2}{2\sigma^2}\right). \quad (3)$$

The parameter B_G determines the height of the Gaussian bump, σ controls its width, and β changes its location in frequency space. The β value can be converted to period P via $P = e^{-\beta}$.

The third model, M3, is used to categorize spectra which flatten off at both the high- and low-frequency ends. It features a kappa function and like M2, it is found by giving the red-noise model three additional parameters:

$$M3 = M1 + B_K \left(1 + \frac{f^2}{\kappa\rho}\right)^{-\frac{\kappa+1}{2}}. \quad (4)$$

B_K gives the size of the kappa function, κ describes its width, and ρ determines its extent into the high-frequency end of the spectrum.

3.1.3 Determination of preferred model

For each input signal, we seek the model which best describes the shape of the spectrum, which we refer to as the ‘preferred model’. A preferred model of M2 means that oscillations are detected in the given timeseries which are unlikely to be a manifestation of noise. Each spectrum is fitted with all three models, and a weighted residuals squared (WRS) value for each fit is obtained. For the weighting values, we use the global wavelet spectrum (GWS),

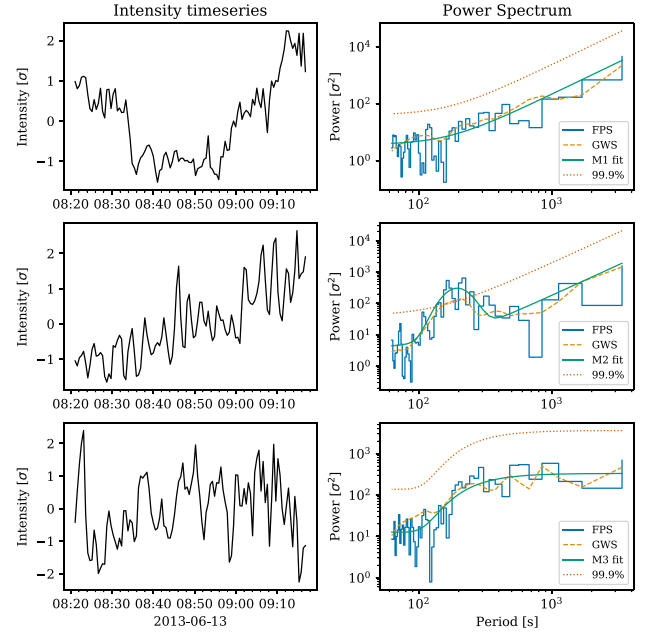


Figure 7. A selection of Ca II 8542 Å intensity timeseries, giving examples of each of the three spectrum models. Each row contains a timeseries and the corresponding Fourier power spectrum (FPS) for: red-noise, M1 (top row); red-noise with Gaussian bump, M2 (middle row); kappa function, M3 (bottom row). For each spectrum, the FPS is shown by the stepped line, the solid line shows the fitted model, the dashed line is the global wavelet spectrum (GWS), and the dotted line is the 99.9 per cent significance level.

following Auchère et al. (2016), as this is a good proxy for the overall shape of the Fourier spectrum.

Because two of the models have more parameters than the other, an F-test is used when comparing the models. The F-statistic for two models is defined as

$$F = \frac{\left(\frac{WRS_1 - WRS_2}{k_2 - k_1}\right)}{\left(\frac{WRS_2}{N - k_2}\right)}, \quad (5)$$

where k is the number of parameters per model ($k = 3$ for M1 and $k = 6$ for M2/M3) and N is the total number of data points in the fit. The null hypothesis for this test is that M1 describes the spectrum as well or better than M2 or M3, and a p-value to reject it is found from the $F(k_2 - k_1, N - k_2)$ distribution.

If a spectrum is determined from the F-test to be best described by M2, the height of the Gaussian bump must then be large enough to pass above a significance test based on the level of the background spectrum. The significance level is determined from the background spectrum by first removing the Gaussian element and then multiplying by a factor $m = -\ln(1 - X^{1/N})$ where X is the desired significance level. This expression arises from the fact that the Fourier spectrum is χ^2 -distributed around the mean power level (Auchère et al. 2016). In all of the analyses in this paper, 99.9 per cent was used as the significance level for the F-test and the Gaussian bump height. The main elements of the fitting process can be seen in Fig. 7, where we show example spectra for each spectrum model. For each of M1, M2, and M3, this figure displays an input intensity timeseries from the Ca II 8542 Å data, the resulting Fourier power spectrum, the preferred model fit, the global wavelet spectrum, and the 99.9 per cent significance level.

3.2 Chromospheric velocity measurement

To measure the velocity of material in the chromosphere, we identified Doppler shifts to the line core of Ca II 8542 Å. The data set features a rather narrow wavelength window ranging over ± 0.5 Å, meaning that the maximum velocity shift we can measure is ± 17 km s⁻¹. Flares have been observed to cause velocity flows of the order of 10 km s⁻¹ in lines from the heated upper chromosphere (e.g. Milligan & Dennis 2009) and in the H α line (Wuelser & Marti 1989) but derived velocities in Ca II 8542 Å flare ribbons are smaller, typically only a few km s⁻¹ (Kuridze et al. 2015, 2018). Though 17 km s⁻¹ is the upper limit of the flows we could observe with this Ca II 8542 Å data set, flows above ~ 7 km s⁻¹ would be difficult to ascertain with much confidence, because we do not want to fit too close to the edges of our spectral range. We assume that the typical Doppler shifts will be within the available spectral window, though note that velocity signals in the Ca II K line in the range 10–20 km s⁻¹ have been detected in small flares before (Falchi, Teriaca & Maltagliati 2006; Keys et al. 2011).

Ca II 8542 Å spectral lines in the majority of pixels over the sunspots are in absorption, and in the areas of flare brightening show strong Gaussian emission features. However, in the region around the filament the line shapes are erratic, likely due to complex radiative transfer as light passes through the cooler plasma high in the atmosphere. For this reason, we ignore the areas surrounding the filament in our velocity analysis, instead focusing on the sunspots and the flare ribbon.

The wavelength shift of the core, $\Delta\lambda$, is determined using a second-order polynomial fit over the middle five wavelength points of the line. The quadratic fit is deemed to be good if the sum of the squared residuals is below 2×10^{-3} and the centre of the fit is within the fitted wavelength range. If the fit is bad, another attempt is made, with a three-point fitting window centred on a turning point in the line shape which was closest to the previous shift value. This is in an effort to find strong peaks which were far from the rest wavelength. If the sum of the residuals squared of the second fit is not below 1×10^{-3} or the result is outside ± 0.5 Å then the wavelength shift at that time-step is set to the value of the previous shift. Wavelength shifts were converted to line-of-sight velocities via $v_{\text{los}} = c\Delta\lambda/\lambda_0$. We measured uncertainties in the results of quadratic fits to several selected lines, from which we estimate that typical errors in the velocity values are ± 0.25 – 0.5 km s⁻¹.

3.3 Chromospheric and photospheric magnetic fields

In this data set, the Ca II 8542 Å Stokes Q and U data are too noisy for the determination of the full chromospheric magnetic field vector. Using the I and V data, we can construct maps of the line-of-sight magnetic field component in the chromosphere using the weak field approximation (WFA; Degl'Innocenti & Degl'Innocenti 1973). The WFA is an approximate solution to the radiative transfer equation which allows the relation of Stokes Q , U , and V to derivatives of Stokes I . The line-of-sight field B_{\parallel} relates V to the gradient of I (Degl'Innocenti & Landolfi 2004; Asensio Ramos 2011)

$$V_{\lambda} = C_1 f_B B_{\parallel} \frac{\partial I(\lambda)}{\partial \lambda}. \quad (6)$$

Here, $C_1 = -4.67 \times 10^{-13} \bar{g} \lambda_0^2$ with the effective Landé factor $\bar{g} = 1.10$ and f_B is the magnetic filling factor, which we set to unity.

For each pixel in the Ca II 8542 Å data, the line-of-sight field strength was found which minimized the difference between the two sides of equation 6.

The Fe I 5250 Å data were not as noisy as Ca II 8542 Å, meaning we were able to analyse the full magnetic field vector at the photosphere. The photospheric field was measured using inversions of the Fe I 5250 Å data under the Milne–Eddington approximation (de la Cruz Rodríguez 2019).²

4 RESULTS

4.1 Chromospheric intensity oscillations

In this study, we compare oscillations detected before and after the flare activity by choosing two 55 minute time intervals over which to perform separate analyses. The two intervals cover 08:21 to 09:17 and 10:03 to 11:00, and will be referred to as ‘pre-flares’ and ‘post-flares’, respectively. Intensity timeseries from individual pixels across the CRISP field-of-view in these two time intervals were analysed using the spectral fitting method described above. The same process was applied to wavelength points spanning the spectral line in five sections: line core, near blue/red, and far blue/red. Fig. 8 shows which of the three spectrum models was preferred for pre- and post-flare timeseries, drawn from Ca II 8542 Å intensity data. The underlying sunspot umbrae are displayed by contours, which were determined by 40 per cent of the maximum intensity level of a single Fe I 5250 Å image. Coloured patches show the pixels where the flare heating is most evident, based on their maximum intensity in Ca II 8542 Å.

The most common result across all pixels is the red noise spectrum model (M1). This was expected as this represents the ‘default’ result of the fitting process, and indicates a spectrum with no strong oscillatory signals. There is a small proportion of pixels assigned to the kappa-shaped spectrum model (M3), and these seem to be more prevalent further towards the wings of the line. The kappa-model pixels are slightly more concentrated towards the edges of the field of view, away from the sunspots and pores.

There is a significant number of pixels for which the Gaussian bump model was preferred, which are seen mostly across the middle of the field of view, covering the active region. The M2 pixels – which are indicators of oscillations – are more prevalent at the line core. There are concentrated areas of intensity oscillation signals in the blue and red sides of the line but they cover much smaller areas. For example, sunspot B is almost completely covered by M2 pixels in the pre-flares line core results, spanning approximately 100 pixels across, while in the far red results the M2 pixels at the same sunspot span ~ 25 pixels. The pixels exhibiting oscillatory signals are mostly around the positions of magnetic activity across the middle of the field of view, which follows very closely the magnetic pores, as well as the bright ribbon structure which was illuminated during the flares.

It can be seen that there are some differences when comparing the pre-flares results to the post-flares in Fig. 8. Over sunspots A–D to the right of the field of view there is a much larger area of M2 fits before the flare activity, when it extends further over the edges of the sunspot umbrae. This is clear to see for sunspots A and B when comparing the results from line core data at both time intervals.

A band of intensity oscillations near the (eventual) flare ribbon extends along the active region from $x = 800$ to 1100 in the pre-flares line core and near-blue/red results, whereas in the post-flares interval this long band is no longer present at these wavelengths. There is however some concentration of oscillatory pixels along the flare-heated ribbon in both the near-red and far-red wavebands after

²<https://github.com/jaimedelacruz/pyMilne>

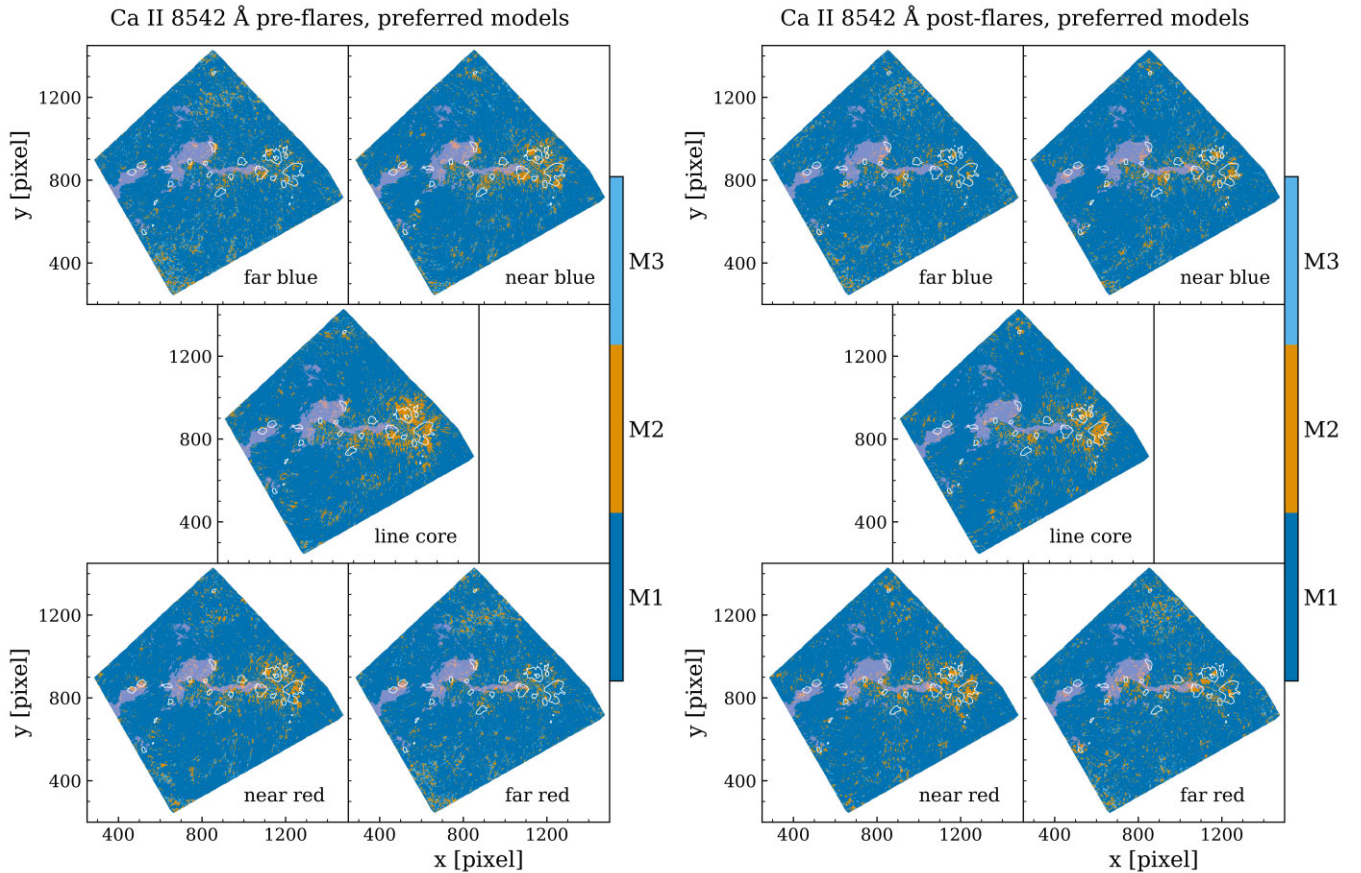


Figure 8. Intensity oscillations: the preferred spectrum model for each pixel of Ca II 8542 Å in the pre-flares (left) and post-flares (right) intervals. The underlying sunspot umbrae are shown by the solid contour lines – determined by 40 per cent of the maximum intensity of the line core of Fe I 5250 Å. The locations of flaring pixels are shown by the filled contours, and have been determined by the maximum brightness of each pixel. The labels in the lower right of each panel show the part of the spectral line sampled.

the flares. At sunspot C, there is an area of strong post-flares signal at red wavelengths, approximately 50 pixels across, that is cospatial with the western tip of the flare ribbon. At the southern edge of this sunspot there are signals detected in pre-flares data but these are more prevalent at the line core and in the blue wavelengths.

4.2 Periods of chromospheric intensity oscillations

For pixels which are determined to be fitted best by M2, the periods at which the bumps in their spectra peak are shown in Fig. 9. In this figure, the field of view has been changed to focus on the group of sunspots where the majority of intensity oscillations were detected. Over the main sunspots, we see that there is a pattern – the typical periods increase as distance from the centre of the umbrae grows. The range of periods is from 150–200 s in the middle of the sunspots to over 300 s in the surrounding penumbral areas. At the line core, there is a small number of pixels far from the sunspots with periods above 400 s (not shown in Fig. 9). This contrasts with wavelengths towards the wings of the line, where there is a more significant number of M2 pixels in the surrounding quiet regions, the periods of which are typically much shorter (100–200 s). Along the belt of trailing sunspots, periods are typically 200–300 s, and this is the same across the wavelength bands.

We can see from Fig. 9 that the locations of the oscillatory signals are often different in the post-flares interval than in pre-

flares, making direct comparison difficult, especially towards the line wings. However a comparison is possible where the concentration of oscillatory pixels is greatest, in the line core over the two largest sunspots (A and B). For example at sunspot A, oscillations around the edge of the umbra had periods of ~ 150 s in pre-flares data, and ~ 250 s after the flares. It appears that the area containing oscillations at the western side of sunspot A moved as a whole towards the centre of the sunspot group. This means that the same spatial location is displaying an increase in the typical periods from, for example, 200 to 300 s at the umbral border, while the 200 s signals appear inside the umbra. The periodicities over sunspot B’s umbra appear to have, on the whole, increased, with the lowest period signals of ~ 100 s disappearing in the post-flares interval.

The periods of the post-flares oscillations detected above sunspot C at the end of the flare ribbon are approximately 150–200 s and are visible in the near red, far red, and near blue wavelengths. There are some oscillations near sunspot C in the pre-flares data however they are located at the lower part of the umbra, and their periods are significantly higher at 250–300 s.

4.3 Chromospheric velocity oscillations in the sunspots

Chromospheric velocity timeseries were obtained for each pixel over the pre-flares and post-flares intervals, by the method described in Section 3.2. We searched for oscillatory signals in the timeseries

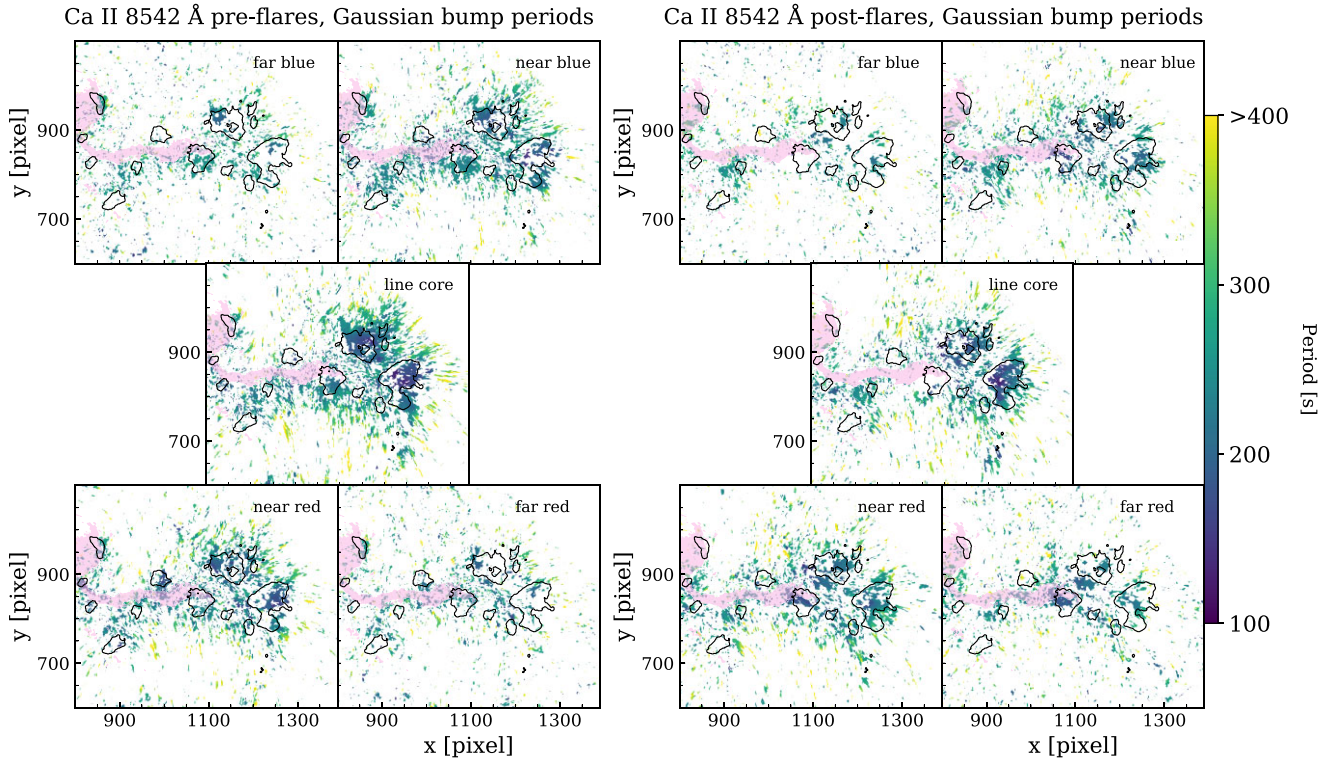


Figure 9. Intensity oscillations: the period at which the Gaussian bump peaks for Ca II 8542 Å timeseries in the pre-flares (left) and post-flares (right) intervals when M2 was the preferred model. The plots cover the same spatial extent as in Fig. 8, in order to focus on the group of sunspots with its high concentration of M2 model pixels. The underlying sunspots are shown by the solid contour lines, determined by 40 per cent of the maximum intensity of the Fe I 5250 Å line core. The locations of flaring pixels are shown by the filled contours, and have been determined by the maximum brightness of each pixel.

using the same spectral fitting method as for the intensity oscillations, again using a 99.9 per cent significance level. We show in Fig. 10 the preferred models and Gaussian bump peaks for velocity timeseries from Ca II 8542 Å. This figure contains both the pre- and post-flares data and the spatial limits are the same as in Fig. 9, focusing on the sunspot group and the long flare ribbon. We avoid the area with the large filament on the left of the CRISP field of view because the line shapes were extremely irregular for much of this location and its surrounding area. Assigning a single velocity value to these spectral lines would not be fruitful because of the absorbing material moving above the chromospheric material below.

From the upper two panels of Fig. 10, we can see that, similarly to the intensity analysis, the red noise model is preferred for most of the velocity power spectra. There are concentrations of velocity oscillations detected around the main sunspots to the right of the field, and there is also a band of oscillations detected along the trail of pores in the centre, south of where the strongest flare heating occurred. For this band of signals, its location is approximately the same when comparing the pre- and post-flares results; however, in the post-flares data, its area seems contracted into a narrower channel. The contraction is displayed by the values of the Gaussian bump peak periods (Fig. 10 lower panels) as the longer period signals move upwards in the field of view after the flares.

The sunspot oscillations look quite different in the velocity analysis, compared to simple intensity at the line core. Sunspot B contains many detectable velocity signals in the pre-flares interval within the umbra and around its upper-right edge. In the post-flares data, however, the penumbral signals remain and the umbral velocity

oscillations are no longer detected. Over sunspot A, the opposite happens: the umbra is clear of velocity oscillations in the pre-flares interval but there are penumbral signals which seem to move inwards towards the spot centre after the flares.

In terms of the typical periods of velocity oscillation (lower panels of Fig. 10), the peaks of the spectral bumps show the same pattern as the intensity signals, of increasing periods with distance from the umbral centre. We can see this in sunspot B with periods as low as 100 s in the middle of the sunspot. At the edges of this sunspot, the periods are 200–300 s and outside the vicinity of the sunspot, we see periods approaching 400 s.

4.4 Chromospheric velocity oscillations in the flare ribbon

There are signals present in the pre-flares interval along the edges of the flare ribbon's eventual location (shown as the lilac patch in Fig. 10), but in the post-flares interval velocity oscillations are detected along the flare ribbon itself. There is a large concentration of oscillations after the flares at the ribbon near sunspot C, and also a broken line of oscillations following the ribbon between $x = 900$ and $x = 1000$. There do appear to be signals close to the ribbon in the pre-flares data but these have moved significantly in the post-flares interval. There is a presence of oscillatory signals at sunspot D, just north of the flare ribbon, in the pre-flares interval, but little to none in the post-flares data at the same location. The signals at sunspot D before the flares are similar in period to the ones located at the end of the ribbon in the post-flares interval (100–200 s).

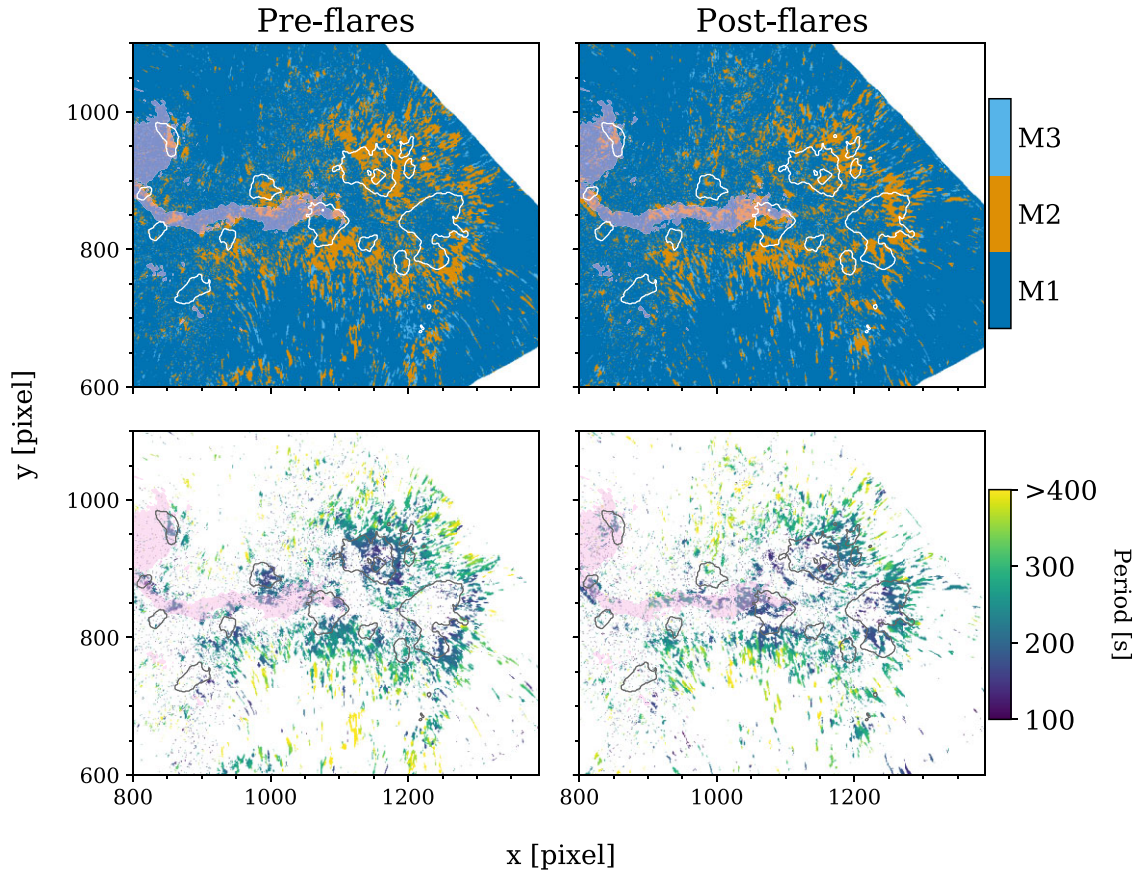


Figure 10. Velocity oscillations. Top row: the preferred power spectrum models in velocity timeseries drawn from Ca II 8542 Å. Bottom row: periods where the Gaussian bumps peak for pixels where M2 was the preferred model. The left column is from the pre-flares interval and the right column is post-flares. The underlying sunspots are shown by the solid contours and the flaring pixels by the filled contours. The field of view is cropped to avoid the dynamic filament to the east.

4.5 Intensity versus velocity oscillations in the chromosphere

By comparing Fig. 9 to Fig. 10, we can investigate which properties are shared between the intensity and velocity oscillations. For example, at sunspot B, the loss of periodic signals after the flares is clear to see in both velocity and line core intensity. Before the flares, along the southern edge of the flare ribbon there is a long band of intensity oscillation signals in the line core and near-blue, but after the flares there are few intensity oscillation signals at this location. In contrast, velocity oscillations are detected along this band in both the pre- and post-flares intervals.

The velocity signals near the flare ribbon in both time intervals seem to correlate well with signals in near-red intensity, both in their locations and typical periods. For example, see the signals at sunspot D in the pre-flares interval, and near sunspot C in the ribbon in post-flares data.

The line core intensity oscillations near sunspot A seem to move ‘inwards’ after the flares, covering more of the umbra. In the velocity results, there are almost no signals detected over the umbra in pre-flares data but there are some around its outer edge. After the flares the velocity signals are around the inside of the edge of the umbra. This seems to mimic the inward movement of the intensity signals but with the velocity signals lagged spatially.

In terms of the properties of both kinds of oscillation, we can see that the periods observed in velocity data are of a similar order as the intensity variations, typically 100–400 s. This coupled with the

fact that velocity signals are also concentrated in the vicinity of the sunspots suggests that they are related to the same phenomenon as the intensity signals. We discuss the relation between intensity and velocity oscillations more in Section 6.1.

5 EVOLUTION OF THE ATMOSPHERE

Here, we explore how the active region changed during the course of the observations in order to gain an understanding of the possible cause of the changes to the oscillatory signals which were detected.

5.1 Intensity imaging

The morphology of the active region can be seen in Fig. 11, featuring Fe I 5250 Å wing and Ca II 8542 Å core intensity images at several epochs showing the photospheric and chromospheric features. The images sample times at the beginning of the observations (in the pre-flares interval), just after the brightening of the ribbon by the second flare, and at the end of the CRISP observation.

There is a lot of movement of the sunspot umbrae, which is visible in the Fe I 5250 Å images, particularly for the very small magnetic pores which can be seen to change positions entirely over the length of the observation. For the largest sunspots, their shapes change noticeably, particularly around their edges, and we can see the

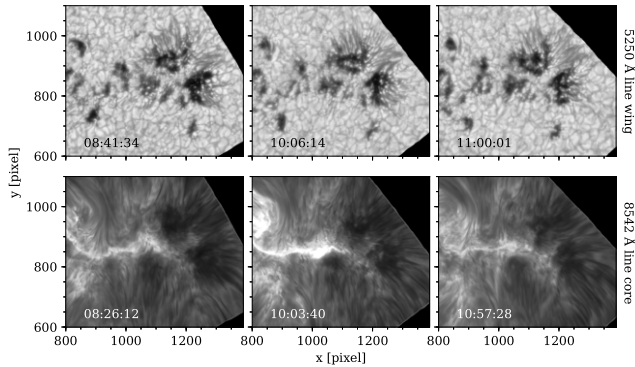


Figure 11. Intensity from the wing of the Fe I 5250 Å line (top row) and line core intensity of Ca II 8542 Å (bottom row) at several time instances, indicated in the lower left of each panel. The colour scales for each row are constant.

appearance and disappearance of bright kernels within the umbrae. We can also see that the penumbrae of the sunspots change over this interval with some locations appearing more ‘penumbral’ such as the area between sunspots A and B.

The chromosphere does not exhibit large-scale obvious changes in the same way. We can see that the shape of the bright ribbon structure changes, seeming to extend further down (in the y -direction) into the space between sunspots A–C. Above the three largest sunspots, the chromosphere appears dark, with many strand-like fibrils visible. A noticeable change is that the dark areas over the sunspots appear to be more physically extended in the earlier image than in the images from after the flares.

5.2 Magnetic field

Over the length of the observation (2.5 h), the features of this active region moved approximately 1.5 deg around the solar rotation axis. This would slightly affect the measurement of the magnetic field with respect to the line-of-sight, but not by much.

5.2.1 Chromospheric field strength

In the top row of Fig. 12, we show how the line-of-sight field measured with the Ca II 8542 Å data changed over the course of the CRISP observation. The result at each value of time was averaged over a 6 minute interval, and a Gaussian smoothing filter was applied in space to remove outliers and noisy pixels when calculating the differences.

The first panel of the top row of Fig. 12 shows the chromospheric field at the start of the observations, and in this active region the field along the line-of-sight is measured as positive almost everywhere. This means that the sunspots are dominated by flux pointing towards the observer. The field is as strong as 1.2 kG over the largest sunspots, and is in the range 500–1000 G in the immediate vicinity of the umbrae. Outside the active region the line-of-sight component of the field is much weaker, typical values are 50–150 G within the area shown in Fig. 12, except for a small area to the west of sunspot A which is weakly negative, as low as -150 G. This suggests that the field is weak or mostly horizontal outside of the sunspot group. In the following three panels, we see how the line-of-sight field strength changes over the course of the observation. The first difference image is from towards the end of the pre-flares interval, the second is from just before the second flare peak, and the last is from the end of the

post-flares interval. There are significant changes to the measured line-of-sight field strength, by as much as $\Delta B_{\parallel} = \pm 400$ G at some locations. Outside of the areas with the largest field changes, small fluctuations of the order of ± 10 G are observed. Since the field is positive almost everywhere at the beginning of the observations, increases in the line-of-sight field strength could imply that the field is becoming more closely aligned to the sight line, and less inclined. Likewise, decreases in the line-of-sight field likely correspond to an increase in field inclination angle. For instance, around sunspot A, the area to the right of the umbra shows large reductions to the line-of-sight field strength, which is likely the field becoming more inclined, and hence more ‘penumbral’. In the first difference image (09:07:11), the umbra of this sunspot shows slightly positive field changes; however, in the latter two difference images the majority of the umbra shows strong decreases from the initial state.

Some of the chromospheric field changes in the latter three time instances seem to exhibit a spatial shift as time passes. We can see this, for example, in the umbra of sunspot A as the diagonal strip of positive field changes, moves from right to left, or over sunspot D where a large patch of negative difference moves right to left, engulfing the sunspot umbra. This is not a systematic effect as it is not seen over the entire field of view.

Although there can often be strong field changes associated with flare activity, the gradual nature of the changes here are perhaps more likely due to the evolution of the active region and changing shape of sunspots.

5.2.2 Photospheric field inclination

The photospheric magnetic field inclination was measured using the Fe I 5250 Å data by performing inversions under the Milne–Eddington approximation. The lower row of Fig. 12 is similar to the upper row, but showing changes to the magnetic field inclination with respect to the line-of-sight returned by the inversions. As seen in the first panel, the field inclination is low over the sunspots, with the lowest values near sunspot B. The area surrounding the active region is mostly highly inclined fields. Sunspots A, B, and C show increases to the inclination, with measured changes reaching $\pm 35^{\circ}$. There is however a channel separating sunspot A from the others in which the field becomes significantly less inclined as time passes.

The field changes seen in the inverted Fe I 5250 Å data match very closely the chromospheric measurements from Ca II 8542 Å, but there are some features which seem shifted in space when comparing the two heights at the same time. For example, the diagonal feature mentioned above which separates sunspot A from the others in the last difference images is further to the left of sunspot A’s umbra in the photospheric measurements. This most likely illustrates how magnetic features at different heights can appear at different locations due to the inclined field.

In the vicinity of sunspot C where velocity oscillations were observed, we can see that there are chromospheric changes which do not match up with any difference features seen in the photospheric measurements. Over the umbra there is an increase to the line-of-sight chromospheric field strength, but the whole umbra shows that the photospheric field became more inclined. This could be a similar effect as seen by Kleint (2017), who detected chromospheric line-of-sight changes in a flaring active region that in some cases did not appear to be related to photospheric field changes.

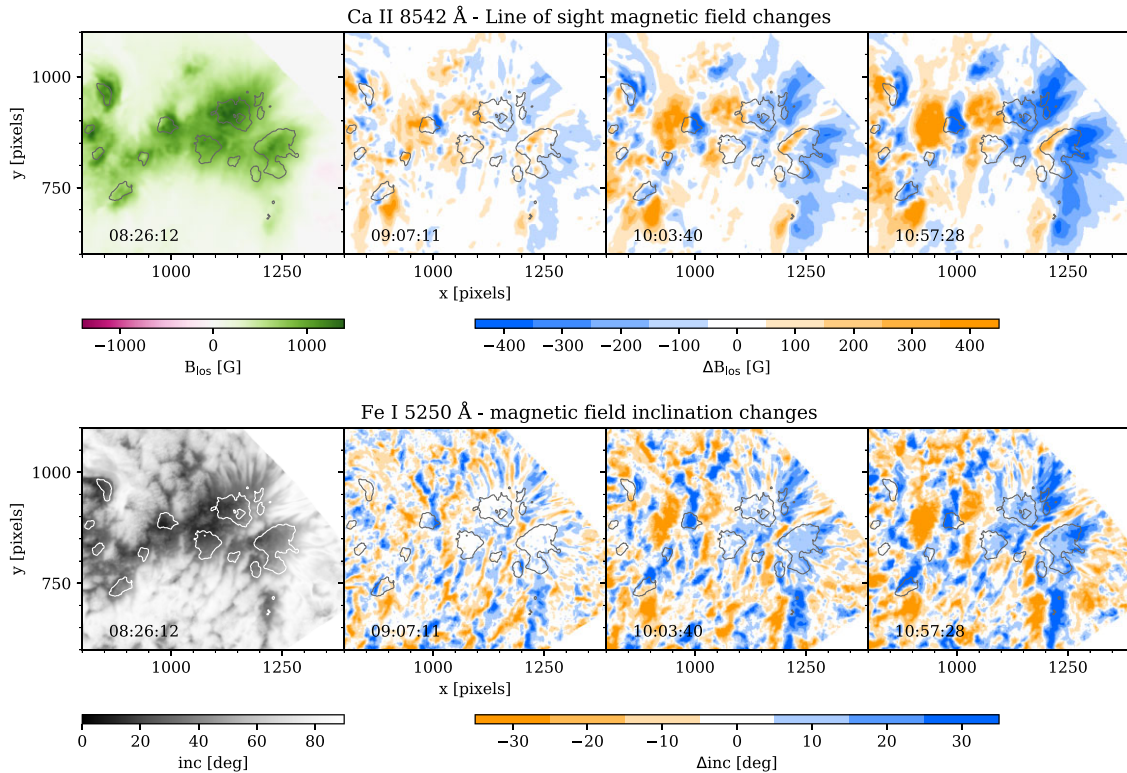


Figure 12. Upper row: the line-of-sight magnetic field as measured by the Ca II 8542 Å using the weak field approximation. The magnetic field values have been averaged in time over a ~ 6 minute interval around the central time, indicated in the lower left of each panel. A Gaussian smoothing filter was applied to each image before the difference calculation. First panel: the line of sight magnetic field strength at 08:26:12 UT, an hour before the flares. Following panels: difference images of the line of sight field, in relation to the first panel, half an hour later (but still pre-flares) at 09:07:11 UT, after the start of the second flare at 10:03:40 UT, and an hour post-flares at 10:57:28 UT. Lower row: inclination of the magnetic field at the photosphere, measured by Milne–Eddington inversions of Fe I 5250 Å data. The panel layout and times are the same as the upper row. Contours show the sunspot umbrae, based on 40 per cent of the maximum Fe I 5250 Å core intensity.

6 DISCUSSION

A summary of the main results from the intensity and velocity oscillations, and the changes to the atmosphere at each named sunspot and the flare ribbon is given in Table 1.

6.1 Sunspot oscillations

In Sections 4.1–4.3, oscillations were identified and contrasted at several wavelengths and over two ~ 55 minute intervals, in both intensity and velocity. The majority of the oscillatory signals were found at the line core of Ca II 8542 Å near the group of sunspots which extend across the middle of the field. There are fewer oscillatory signals at wavelengths away from the core, and this could be for a variety of reasons. Wavelengths further towards the wings originate from lower in the atmosphere than at the core, but in some cases, they can also be emitted from a larger slab of the atmosphere, for example in RADYN flare simulations of the Ca II 8542 Å line (da Costa et al. 2015; Kerr et al. 2016). It is therefore possible that the oscillations are not predominant in the lower parts of the atmosphere, or that the signals are harder to detect because the light we receive is from a large range of heights, leading to incoherent signals. Another possibility is that in the lower atmosphere where mass density is higher wave amplitudes are lower due to conservation of energy. The lower amplitude waves at deeper layers could therefore be more difficult to detect.

We saw that in intensity data, there was a reduction in the area covered by oscillatory signals around the largest sunspots: signals remained present in the umbrae but had disappeared in the penumbrae after the flares. From intensity images (Fig. 11), we see that the penumbral areas over sunspot A and B changed in appearance. The dark area over the sunspots in the chromosphere became less extensive, and this coupled with the magnetic field changes showing more inclined fields (Fig. 12) suggests that the area surrounding the sunspots has become more ‘penumbral’ than ‘umbral’. This means that the local cut-off period will have been altered which could explain the lack of intensity oscillations. It is also possible that the oscillations are present but no longer detectable, either because the heights of oscillatory signals changed or the heights sampled by the Ca II 8542 Å line had been altered.

The typical periods of the intensity oscillations follow a well-known pattern of period increasing with distance from the centre of the umbra, often referred to as running penumbral waves (Jess et al. 2013). This is thought to be due to increased cut-off periods caused by increasing magnetic field inclinations, which is consistent with the magnetic field measurements shown in Fig. 12. There were also some variations in the periods when comparing pre- and post-flares intervals, for example on the western border of sunspot A, periods were seen to increase from 100–150 to ~ 250 s. The magnetic field was seen to become more inclined over time, which explains this observation. It is, however, unclear if the magnetic field changes

Table 1. Summary of the main oscillatory results from full-resolution Ca II 8542 Å intensity (Fig. 9) and velocity (Fig. 10), with noted changes to the atmosphere which are visible in Figs 11 and 12.

Location	Pre-flares intensity oscillations	Post-flares intensity oscillations	Pre-flares velocity oscillations	Post-flares velocity oscillations	Atmospheric changes
Sunspot A	Cover most of west umbra. Periods at umbral centre 100–200 s, increasing radially.	Area covered shifted inwards over umbral centre. Co-spatial periods increase.	No umbral signal. Concentrated outside of the west umbral border. ~200 second periods.	Oscillations move inwards. Co-spatial periods increase.	Umbral area appears to decrease after flare in Fe, Ca II 8542 Å. Inclination increase by 25°.
Sunspot B	Cover umbra and north/west penumbra. Periods 150–250 s.	Umbra and penumbra covered but much sparser. Loss of lowest period (100 s) signals.	Umbra and penumbra covered. Periods 100–250 s.	Very reduced area over umbra. Penumbra relatively unchanged. Similar periodicities.	Growing penumbra to west in Fe images. Inclination increases +30° over penumbra.
Sunspot C	Dense coverage over southern part of umbra. Periods 200–250 s.	Signals present only in near- and far-red line wings where umbra overlaps flare ribbon. Periods ~200 s.	Coverage to the south of umbra. Periods >250 s.	Signals at umbral locations overlapping flare ribbon. Periods 150–200 s.	Photospheric and chromospheric fields do not agree. Shape of spot changes in Fe image.
Sunspot D	Covered umbra, only in near-red wavelengths.	No signals.	Umbra covered. Periods ~150 s.	No signals.	Sunspot moves eastward, from Fe images.
Flare ribbon	Signals in long band to the south of the ribbon pixels.	Band of signals is gone. Signals partially along ribbon in near- and far-red wavelengths.	Some signals surrounding the horizontal band of flare pixels. Periods 250–300 s.	Band of signals contracts. Dense area over flare pixels near sunspot C, 150–200 s. Concentrated signals trace ribbon with higher periods.	Some movement of underlying magnetic pores visible in Fe.

were directly due to the flares, as the inclination seems to be gradually increasing across each time instance displayed in Fig. 12.

The velocity oscillations which were observed in Ca II 8542 Å were similar to the intensity oscillations in appearance (for instance they follow the similar running penumbral wave pattern), but were in some ways different from the intensity oscillations. For example, there was a lack of velocity oscillations in sunspot umbrae which were almost completely covered by the intensity oscillations. This can give insight into the physical conditions giving rise to these different types of oscillations, but might be highlighting problems in the analyses.

A velocity oscillation which spans the entire spectral window centered on the rest wavelength would produce intensity oscillations at every wavelength step, and oscillations in either wing would be a half-cycle out of phase. The intensity oscillations in the red sections of the post-flares Ca II 8542 Å data co-spatial with velocity oscillations suggest that the velocity oscillation is centred on the red side of the line. The presence of intensity oscillations without corresponding velocity signals could be indicative of intrinsic temperature or density fluctuations which are not related to movement of the plasma. Alternatively, movement perpendicular to the line of sight could cause intensity variations without detectable velocity signals.

Velocity oscillations are most easily detectable when the spectral line has a consistent and simple shape, for instance a Gaussian-like emission or absorption feature close to the centre of the spectral window. It is therefore easy for a coherent velocity oscillation to be interrupted if the line becomes more complex – due to a steep velocity gradient, an absorption feature in the line-of-sight or a large Doppler shift. This explains why there are few signals observed near the large filament structure (and why it was mostly ignored for the velocity analysis), and perhaps why some of the sunspot umbrae are void of oscillatory signals (because of, for example, umbral flashes). It is important to keep this in mind because it means that there could

be oscillations which are not detected by this analysis. However, this does not mean there is any tendency for false positives, only false negatives, in the velocity analysis. Complex line shapes are not as big of an issue for the intensity analysis, a possible explanation for the prevalence of intensity signals, and for situations where there are intensity oscillations with no velocity signals detected (for example in the umbra of Sunspot A).

6.2 Flare ribbon oscillations

The ribbon of the second flare is not typical, because the physical structure which was brightened by the second flare was already present in the active region before the flares began. The bright area running along the centre of the field of view moves subtly over the course of the observations (see Fig. 11). The first flare did cause some activity along this ribbon, but the second flare appears to have had much more impact in terms of chromospheric heating.

There were intensity oscillations detected in the pre-flares interval near the flare ribbon, along its southern edge, near and at the Ca II 8542 Å line core. After the flares there were almost no line core oscillations, but there were strong oscillations in the near and far red wavelengths over sunspot C, which might be evidence of bulk downflows at this location.

The ribbon oscillations are most obvious in velocity data. There are signals south of the bright structure in both pre-flares and post-flares intervals, and in the post-flares interval there is a strong concentration over sunspot C, matching the intensity signals in red wavelengths. The velocity oscillations detected at $x = 850$ – 1025 along the flare ribbon have higher typical periods than the concentration near sunspot C.

We can investigate the velocity oscillations which were detected at the end of the flare ribbon (near sunspot C) in a more in-depth way by analysing timeseries individually. We extracted velocity and intensity timeseries from 10 pixels in a vertical line from the flaring

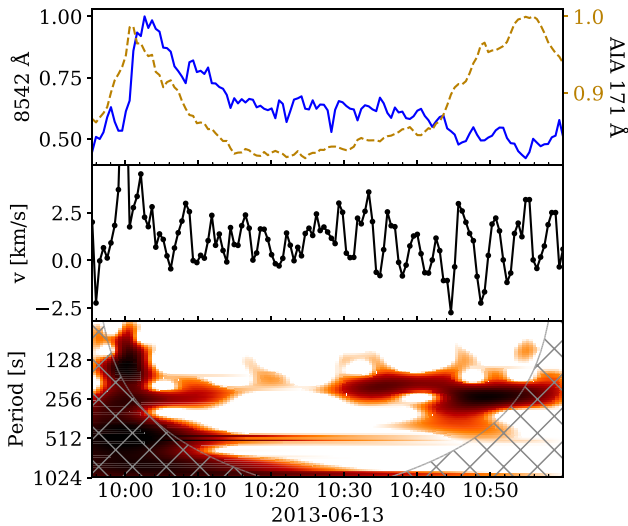


Figure 13. Example of velocity oscillations seen in a flaring pixel, located at $x = 1025$, $y = 852$. Top: the normalized Ca II 8542 Å core (solid line) and SDO/AIA 171 Å (dashed line) intensities starting just before the second flare and extending to the end of the data set. Middle: the line-of-sight velocity as measured by Doppler shift of the Ca II 8542 Å core. Bottom: the wavelet power spectrum of the velocity signal, with a reversed colour scale (high power is dark). The hatched area shows the ‘cone of influence’, where edge effects could impact the spectrum.

area and performed a wavelet analysis. For example, we show one of the velocity timeseries drawn from a pixel at $x = 1025$, $y = 852$ in Fig. 13. Here, we show the Ca II 8542 Å core intensity, measured velocity, and velocity wavelet power spectrum from a time just before the second flare until the end of the data set. The wavelet spectrum was obtained using the method outlined in Torrence & Compo (1998), and is used here to investigate the time-variance of the velocity oscillations. The wavelet colour scale is reversed so dark areas have more power, and we see the clear velocity oscillations reflected in the spectrum. In this example, there is a positive shift in velocity around the time of the rapid intensity increase. This results in high power at the long-period section of the wavelet spectrum at the beginning of the timeseries, though this is under the ‘cone of influence’ of the spectrum meaning the power here may be artificial in nature. There is power at ~ 200 second periods throughout the timeseries (the velocity Fourier power spectrum peaks at $P = 205$ s) but it is most pronounced in the last 30 min. In this latter half hour a clear 3-min periodicity begins at 10:30 and the period grows closer to 4 min from 10:45 onward. Similar strong velocity signals at this time were observed in all of the other pixels in our 10 pixel sample.

The presence of velocity oscillations from 10:30–11:00 coincides with local brightening in the AIA 171 Å as seen in images in Fig. 6 and a timeseries cospatial with the velocity signal shown in Fig. 13. Earlier in the event, at around 10:00 UT, the 171 Å intensity peaked a few minutes before the Ca II 8542 Å core intensity at the same location, before falling rapidly while the Ca II 8542 Å intensity fell more gradually. This first brightening is likely the direct heating of the flare impulsive phase. At 10:30 the 171 Å intensity began to rise steadily to a second peak at 10:55, while the Ca II 8542 Å core intensity continued to fall to the pre-flare level. This second 171 Å brightening may be due to conductive heating of the low-atmosphere plasma from overlying hotter post-flare loops. It is therefore possible that the velocity oscillations are related to the evolution of the post-flare loop and we can speculate on different scenarios leading to

this change of period. Disturbances from the cooling loop – mass movement from chromospheric condensations or waves – could travel down towards its anchor point in the lower atmosphere and could provide an energy source for the resonance of chromospheric ‘3-min’ oscillations. The further increase in period at this location, at around 10:40 UT, could indicate a further change (increase) in the magnetic field inclination, or conductive heating of the deep chromosphere, both of which would result in a decrease in the cutoff frequency (equation 1). Or the observed increase in period could be due to the ‘illumination’ of a deeper layer in the chromosphere, which is oscillating at a lower frequency.

7 CONCLUSIONS

In this paper, we have studied how the oscillatory signatures of this active region changed around the time of two small flares. We found that the positions and typical periods of the oscillations in intensity and velocity were different when comparing times before and after the flare activity. The area covered by oscillatory signals around the sunspots was found to decrease, and the typical periods increased over the penumbra of the largest sunspot. Measurements of the photospheric and chromospheric magnetic fields support the idea that these changes could be due to the magnetic field becoming more inclined, and the penumbrae of the sunspots developing. We found velocity oscillations at the location of flare heating, some of which were cospatial with a post-flare loop near the sunspots which brightened in 171 Å radiation approximately 30 min after the second flare. We speculate that the evolution of the loop could have induced a response from the chromospheric material at its natural resonating frequency.

ACKNOWLEDGEMENTS

The authors would like to thank the anonymous referee for their helpful comments in the improvement of this paper. The Swedish 1-m Solar Telescope is operated on the island of La Palma by the Institute for Solar Physics of Stockholm University in the Spanish Observatorio del Roque de los Muchachos of the Instituto de Astrofísica de Canarias. The Institute for Solar Physics is supported by a grant for research infrastructures of national importance from the Swedish Research Council (registration number 2021–00169). Solar Dynamics Observatory data are courtesy of NASA/SDO and the AIA, EVE, and HMI science teams. PYTHON wavelet software provided by Evgeniya Preddybaylo based on Torrence and Compo (1998) and is available at <http://atoc.colorado.edu/research/wavelets/>. This work was supported by The Carnegie Trust for the Universities of Scotland through PhD studentship PHD007733 (DCLM), Glasgow University College of Science and Engineering (DCLM) and the UK’s Science and Technology Facilities Council (LF) [grant numbers ST/T000422/1 and ST/X000990/1].

DATA AVAILABILITY STATEMENT

Scripts used to generate the results in this paper can be found at github.com/davidclmillar/.

REFERENCES

- Asensio Ramos A., 2011, *ApJ*, 731, 27
- Auchère F., Froment C., Bocchialini K., Buchlin E., Solomon J., 2016, *ApJ*, 825, 110
- Battams K., Gallagher B. M., Weigel R. S., 2019, *Sol. Phys.*, 294, 11

- Bel N., Leroy B., 1977, *A&A*, 55, 239
- Bhatnagar A., Tanaka K., 1972, *Sol. Phys.*, 24
- Chae J., Goode P. R., 2015, *ApJ*, 808, 118
- da Costa F. R., Kleint L., Petrosian V., Dalda A. S., Liu W., 2015, *ApJ*, 804, 56
- de la Cruz Rodríguez J., 2019, *A&A*, 631, A153
- Degl'Innocenti E. L., Degl'Innocenti M. L., 1973, *Sol. Phys.*, 31, 299
- Degl'Innocenti E. L., Landolfi M., 2004, Polarization in spectral lines. No. v. 307 in *Astrophysics and space science library*. Kluwer Academic Publishers, Dordrecht; Boston
- Falchi A., Teriaca L., Maltagliati L., 2006, *Sol. Phys.*, 239, 193
- Farris L., McAteer R. T. J., 2020, *ApJ*, 903, 19
- Fleck B., Schmitz F., 1991, *A&A*, 250, 235
- Inglis A. R., Ireland J., Dominique M., 2015, *ApJ*, 798, 108
- Inglis A. R., Ireland J., Dennis B. R., Hayes L., Gallagher P., 2016, *ApJ*, 833, 284
- Jess D. B., Reznikova V. E., Van Doorselaere T., Keys P. H., Mackay D. H., 2013, *ApJ*, 779, 168
- Kalkofen W., Rossi P., Bodo G., Massaglia S., 1994, *A&A*, 284, 976
- Kerr G. S., Fletcher L., Russell A. J. B., Allred J. C., 2016, *ApJ*, 827, 101
- Keys P. H., Jess D. B., Mathioudakis M., Keenan F. P., 2011, *A&A*, 529, A127
- Khomenko E., Collados M., 2015, *Living Rev. Sol. Phys.*, 12, 6
- Kleint L., 2017, *ApJ*, 834, 26
- Kosovichev A. G., Sekii T., 2007, *ApJ*, 670, L147
- Kuridze D. et al., 2015, *ApJ*, 813, 125
- Kuridze D., Henriques V., Mathioudakis M., van der Voort L. R., Rodríguez J. d. I. C., Carlsson M., 2018, *ApJ*, 860, 10
- Kwak H., Chae J., Song D., Kim Y.-H., Lim E.-K., Madjarska M. S., 2016, *ApJ*, 821, L30
- Lamb H., 1909, *Proc. London Math. Soc.*, s2–7, 122
- Lemen J. R. et al., 2012, *Sol. Phys.*, 275, 17
- Li D., Lu L., Ning Z., Feng L., Gan W., Li H., 2020, *ApJ*, 893, 7
- Millar D. C. L., Fletcher L., Milligan R. O., 2021, *MNRAS*, 503, 2444
- Milligan R. O., Dennis B. R., 2009, *ApJ*, 699, 968
- Milligan R. O., Fleck B., Ireland J., Fletcher L., Dennis B. R., 2017, *ApJ*, 848, L8
- Nakariakov V. M., Foullon C., Myagkova I. N., Inglis A. R., 2010, *ApJ*, 708, L47
- Pesnell W. D., Thompson B. J., Chamberlin P. C., 2012, *Sol. Phys.*, 275, 3
- Rutten R. J., 2020, preprint ([arXiv:2009.00376](https://arxiv.org/abs/2009.00376))
- Scharmer G. B., Bjelksjo K., Korhonen T. K., Lindberg B., Petterson B., 2003a, in Keil S. L., Avakyan S. V., eds, *Proc. SPIE Conf. Ser. Vol.4853, Innovative Telescopes and Instrumentation for Solar Astrophysics*. SPIE, Bellingham, p. 341
- Scharmer G. B., Dettori P. M., Lofdahl M. G., Shand M., 2003b, in Keil S. L., Avakyan S. V., eds, *Proc. SPIE Conf. Ser. Vol.4853, Innovative Telescopes and Instrumentation for Solar Astrophysics*. SPIE, Bellingham, p. 370
- Scharmer G. B. et al., 2008, *ApJ*, 689, L69
- Sych R., Nakariakov V. M., Karlicky M., Anfinogentov S., 2009, *A&A*, 505, 791
- Tan B., Tan C., 2012, *ApJ*, 749, 28
- Threlfall J., De Moortel I., Conlon T., 2017, *Sol. Phys.*, 292, 165
- Torrence C., Compo G. P., 1998, *Bull. Am. Meteorol. Soc.*, 79, 61
- Uchida Y., Sakurai T., 1975, *PASJ*, 27, 259
- Van Doorselaere T., Kupriyanova E. G., Yuan D., 2016, *Sol. Phys.*, 291, 3143
- Wuelser J.-P., Marti H., 1989, *ApJ*, 341, 1088
- de la Cruz Rodríguez J., Löfdahl M. G., Sütterlin P., Hillberg T., Rouppe van der Voort L., 2015, *A&A*, 573, A40
- van Noort M., Rouppe van der Voort L., Löfdahl M. G., 2005, *Sol. Phys.*, 228, 191

This paper has been typeset from a $\text{\TeX}/\text{\LaTeX}$ file prepared by the author.